Supporting Information

Structural Investigations of Au-Ni Aerogels: Morphology and Element Distribution
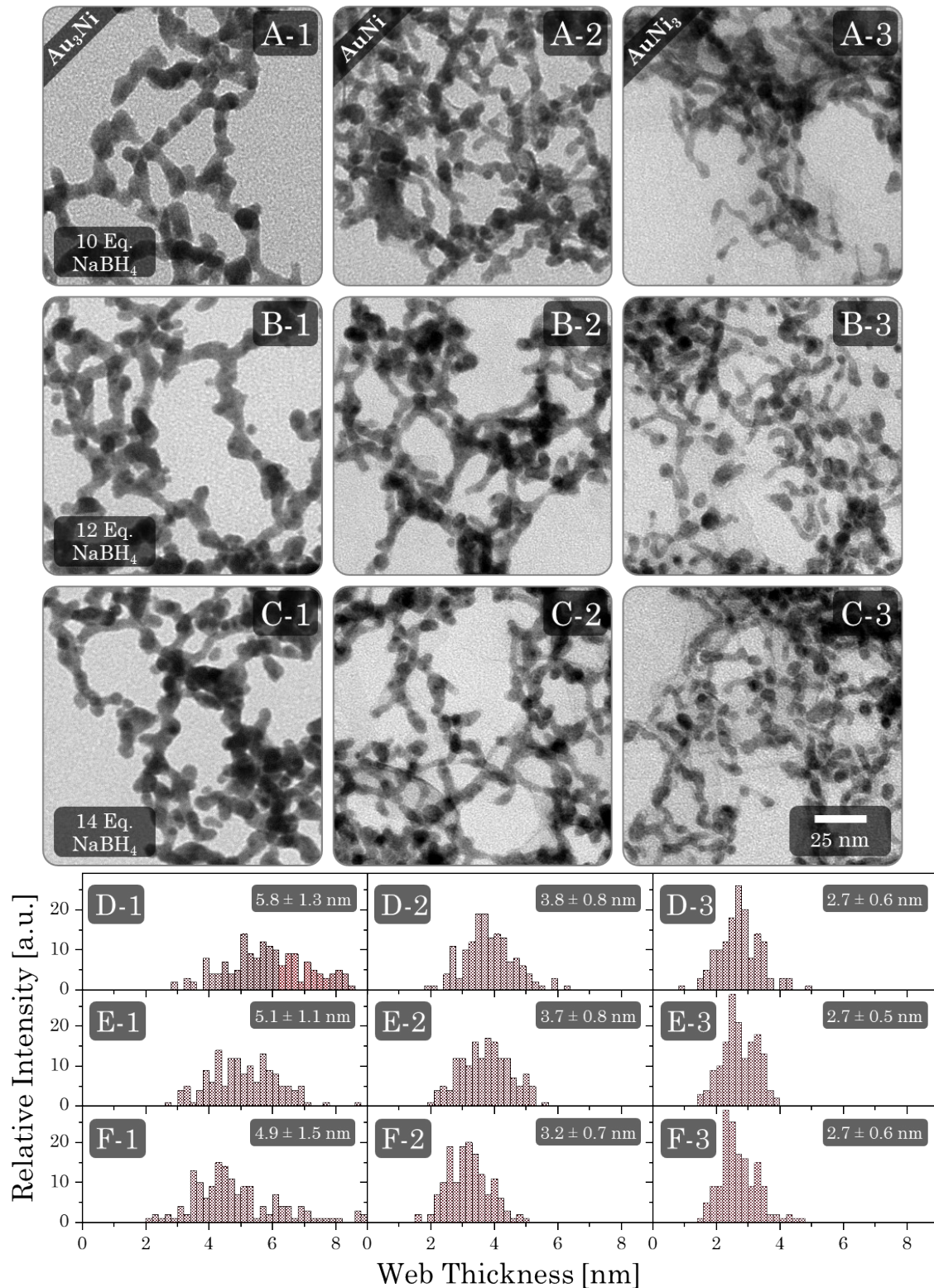
Johannes Kresse,[a] Maximilian Georgi, [a] René Hübner, [b] and Alexander Eychmüller *[a]

[a] Physical Chemistry, TU Dresden, Zellescher Weg 19, 01069 Dresden, Germany.

[b] Institute of Ion Beam Physics and Materials Research, Helmholtz-Zentrum Dresden-Rossendorf e.V.,

01328 Dresden, Germany.

* Corresponding author

E mail: alexander.eychmueller@chemie-tu-dresden.de

Figure 1: TEM micrograph (A-C) and the corresponding ligament size distributions (D-F) of the Au$_3$Ni (1), AuNi (2), and AuNi$_3$ (3) aerogels with a total metal concentration of 0.1 mmol, reduced by 10 Eq. (A, D), 12 Eq.(B, E), and 14 Eq.(C, F) NaBH$_4$. Besides their fine homogeneous structure of interconnected nanochains with small ligament sizes, two size-dependent structural trends become apparent. The ligament size decreases with increasing Ni content and growing NaBH$_4$ excess. Although these changes in ligament size are well within the standard deviation, they are backed up by the slight shift of the distribution curve. At the same time, however, the gel structure becomes increasingly incomplete, exhibiting disconnected nanochains and isolated nanoparticles. The scale bar in C-3 applies to all TEM micrographs.
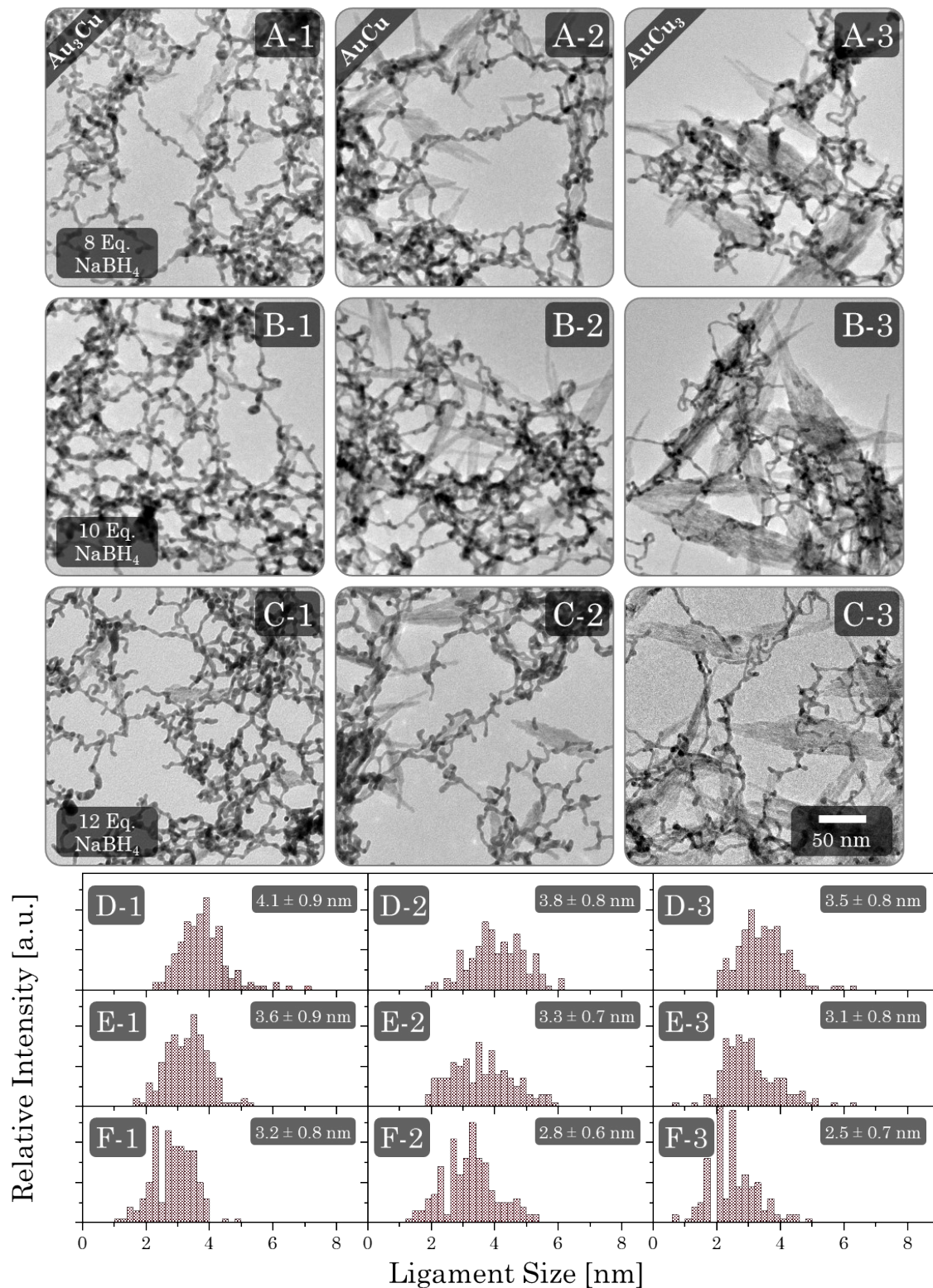
Figure 2 *TEM micrographs (A-C) and the corresponding ligament size distributions (D-F) of the Au$_3$Cu (1), AuCu (2), and AuCu$_3$ (3) aerogels with a total metal concentration of 0.1 mmol, reduced by 8 Eq. (A, D), 10 Eq.(B, E), and 12 Eq.(C, F) NaBH$_4$. They exhibit fine homogeneous structures of interconnected nanochains and small ligament sizes, similar to Au-Ni aerogels. However, instead of incomplete gelation, they display a substructure of copper oxide needles.[1] But most important, they exhibit the same two delicate structural trends as Au-Ni: the decrease in ligament size with increasing Cu content as well as NaBH$_4$ excess, again backed up by the overall shift of the distribution curves. Consequently, both trends can rather be considered for metal aerogels in general. The scale bar in C-3 applies to all TEM micrographs.*
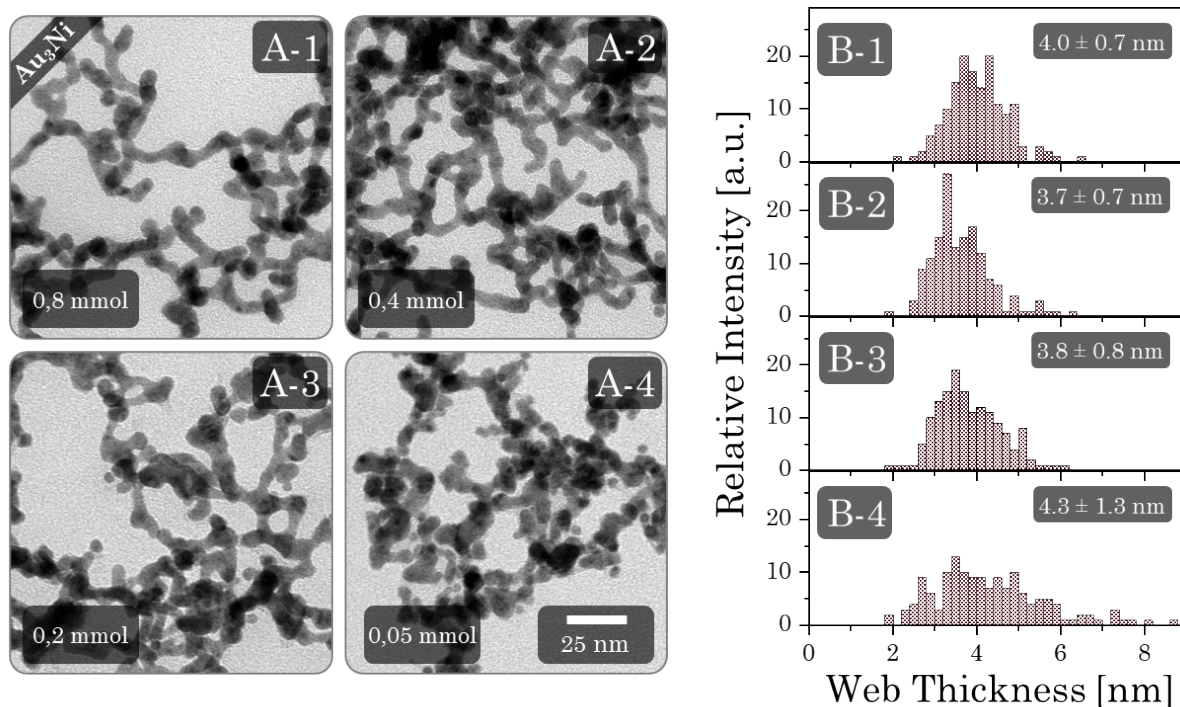
Figure 3: *TEM micrographs (A) and the corresponding Ligament size distributions (B) of the Au₃Ni gels with total metal concentrations of 0.8 mM (1), 0.4 mM (2), 0.2 mM (3), and 0.05 mM (4) reduced by 12 Eq. NaBH₄. Upon increasing the total metal concentration, the ligament size tends to shrink up to 0.4 mM, at which point the trend starts to reverse if continued. The scale bar in A-4 applies to all TEM micrographs.*
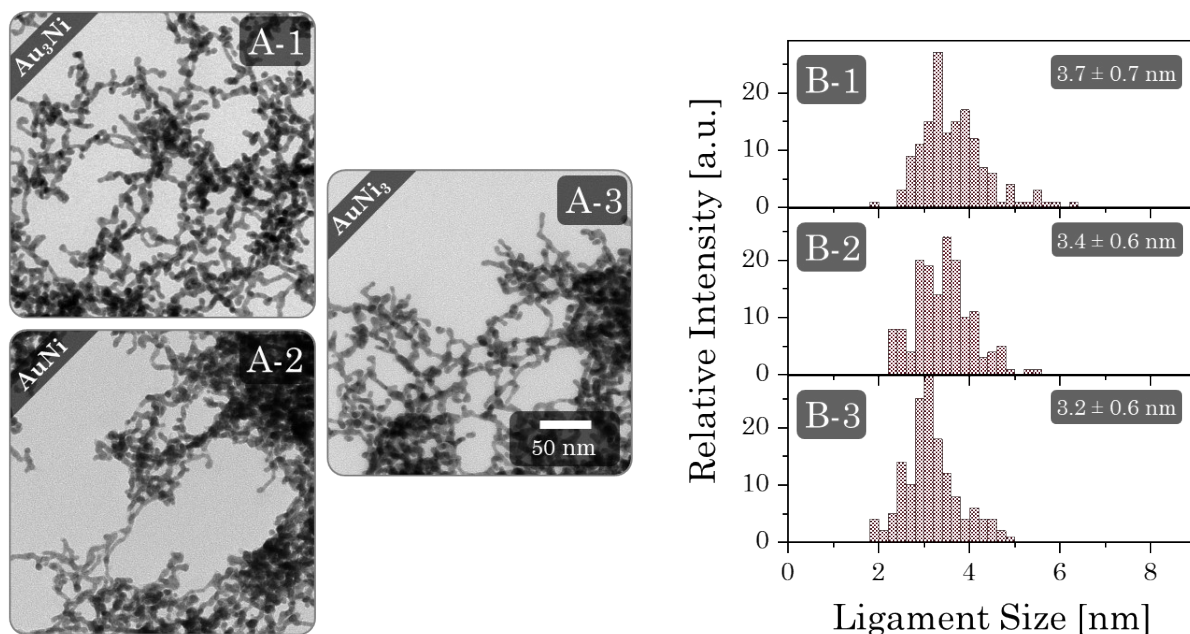
Figure 4: *TEM micrographs (A) and the corresponding ligament size distributions (B) of the Au₃Ni (1), AuNi (2), and AuNi₃ (3) gels with a total metal concentration of 0.4 mM, reduced by 12 Eq. NaBH₄. The resulting gels retain their fine homogeneous structure and a similar ligament size. In conformity with SI Fig. 1, the ligament size tends to decrease from B-1 to B-2 to B-3 according to the increasing Ni content. On closer inspection, samples B-1 and B-2 show a slight tendency to decrease in average ligament size, whereas B-3 increases compared to their counterpart in SI Fig. 1 B/E. This may imply a synergetic dependency between the element composition and the total metal concentration of the resulting structure. The scale bar in A-3 applies to all TEM micrographs.*
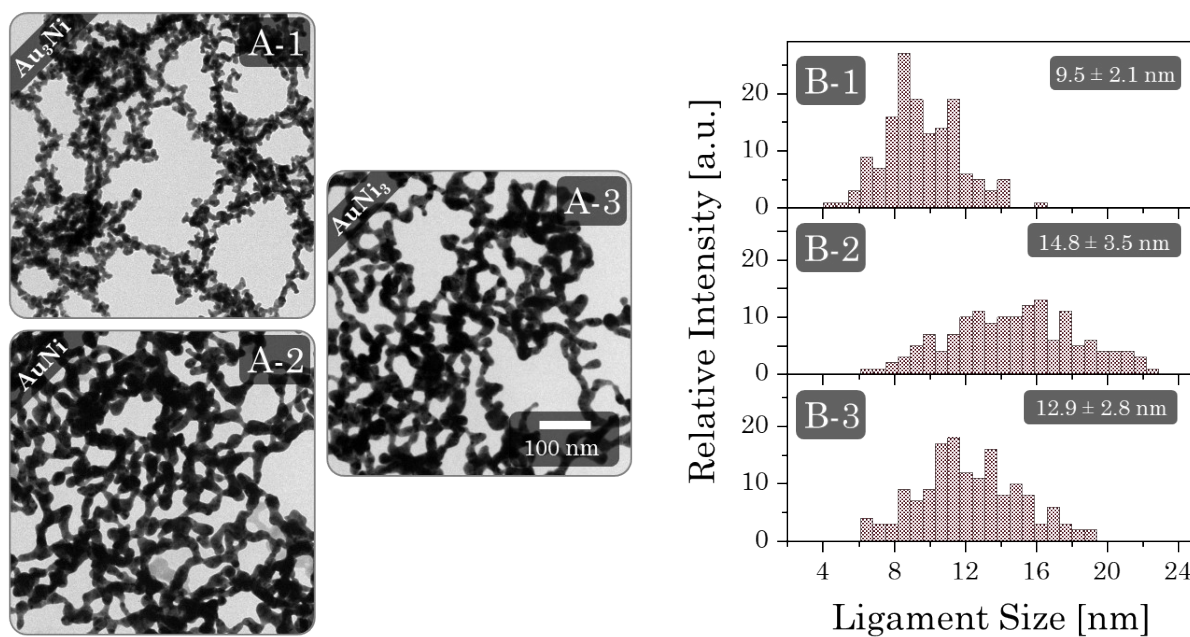
Figure 5: *TEM micrographs (A) and ligament size distributions (B) of the Au$_3$Ni (1), AuNi (2), and AuNi$_3$ (3) gels with a total metal concentration of 0.1 mM, synthesized in EtOH and reduced by 12 Eq. (1) and 4 Eq. (2,3) NaBH$_4$. By changing the reaction medium from water to ethanol, the lower dielectric constant facilitates faster gelation kinetics, resulting in significantly broader ligament size and size distributions for low and high NaBH$_4$ excesses, although the typical gel character is preserved. The scale bar in A-3 applies to all TEM micrographs.*
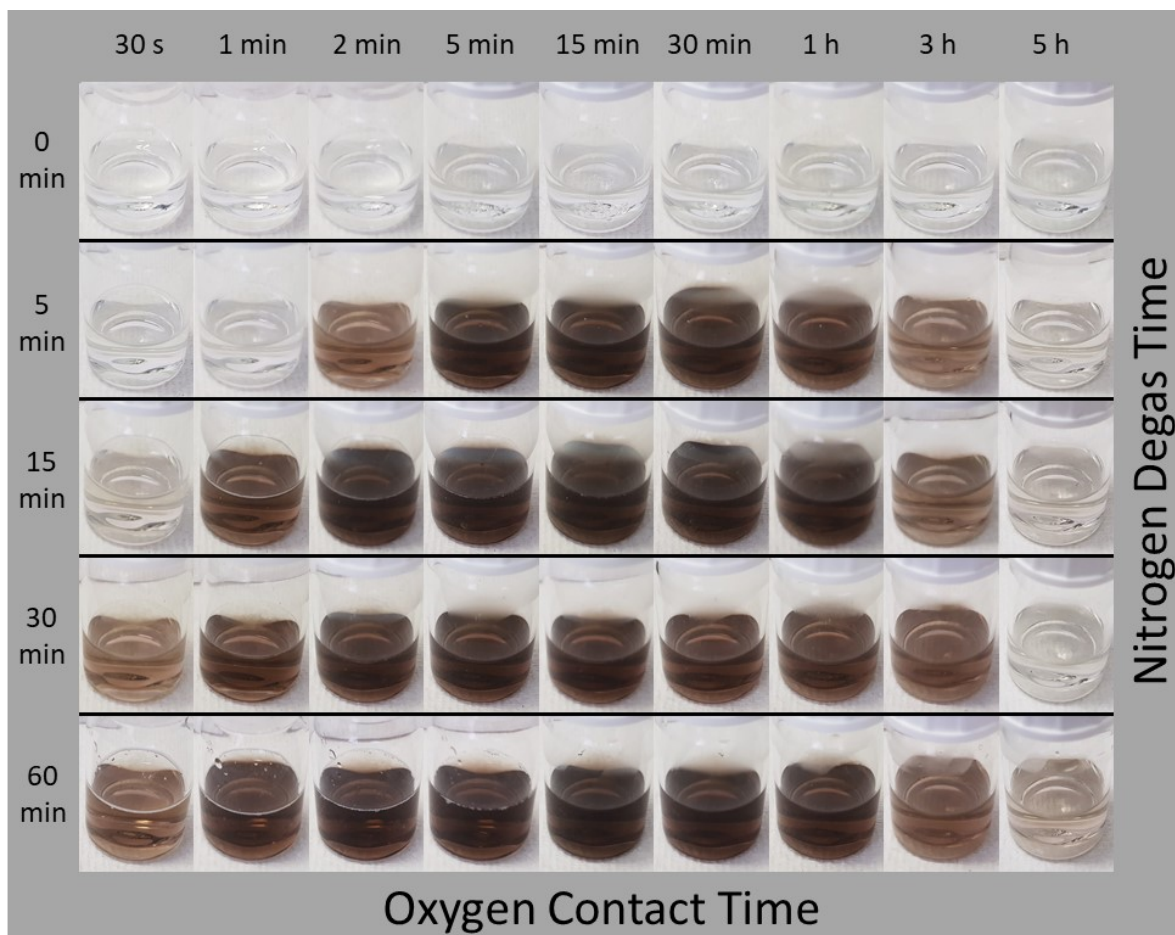
Figure 6: *Stability measurements of citrate-capped Ni NPs in aqueous solution. Ni^{2+} ion solutions were degassed by N_2 perfusion for different times before reduction with $NaBH_4$. At the same time, the nitrogen supply was turned off. Afterward, the color changes were recorded by visual imaging, revealing several important trends. First, regardless of the initial degassing time, all Ni NP solutions were stable for about 1 h before significant discoloration occurred, indicating the oxidation and subsequent dissolution of the NPs. After 5 h, the Ni NPs were almost completely dissolved. Despite this similar behavior, the initial degassing time still has some significance. The longer the degassing time, the faster the Ni^{2+} ions are reduced, and the NPs are formed. It is noteworthy that without degassing, the formation of Ni NPs does not take place at all. Both effects probably lead back to an unwanted side reaction of $NaBH_4$ with air to such an extent that the Ni reduction is suppressed.*

	NH$_4^+$	Cs$^+$	K$^+$	Na$^+$	Li$^+$	Ca^{2+}	Mg^{2+}	Zn^{2+}	Ba^{2+}	Mn^{2+}
CO^{3-}	🔴	🔴		🔴						
SO$_4^{2-}$	🔴			🔴			🟡🟡🟢	⚫		🟢🟢🟢
AcO$^-$				🔴				⚫		🟢🟢🟢
F$^-$	🔴			🟡🟡🟢						
Cl$^-$	🔴	🔴	🔴	🔴	🔴	🟢🟢🟡	🟡🟡🟡🟢	⚫		🟢🟢🟢🟢	🟢🟡🟡🟢
Br$^-$		🔴	🔴	🔴			🟢🟢🟢			🟢🟢🟢
NO$_3^-$	⚫			⚫				⚫		
I$^-$	🟢🔴🔴	🟢🔴🔴	🟢🔴🔴	🟢🔴🔴				⚫		

Cosmo-tropic / Chao-tropic

⚫ Voluminous precipitate which dissolves
🔴 No effect
🟡 Colored gel
🟢 Black gel

Ni NPs | Ni + Au NPs | Au NPs

Figure 7: *Potency of various electrolytes regarding the destabilization of citrate-capped Ni (left dot) and Au NPs (middle dot) as well as the mixtures of both (right dot). If 5 Eq. of electrolyte were not sufficient to destabilize the Ni NPs, the tests were terminated for the respective electrolyte. In addition, not all salts listed were accessible, resulting in blanks. The salts are roughly ordered according to the Hofmeister series, considering the ratio of cosmotrpic (facilitates hydrogen bonds) and chaotropic (hampering hydrogen bonds) properties. In particular bivalent electrolytes and iodine salts are highly effective in destabilizing Ni NPs. All other salts either show no effect or cause accelerated dissolution in the case of zink and nitrate salts. When transferred to Au NPs, bivalent salts were still sufficient to induce gelation, but iodine salts were not. Preferably, salts with higher chaotropic ions transformed the NPs into a black gel, while more cosmotropic electrolytes formed colored gels instead (increased ligament size). When Au and Ni NPs mixtures were destabilized, again only bivalent electrolytes enabled the destabilization, but compared to before, all salts tested yielded black gels. Moreover, NaF was the only monovalent electrolyte that facilitated gelation, though in smaller quantities, as compared to bivalent salts. The sudden formation of solely black gels for the mixed NPs in contrast to earlier colored gels is probably related to co-precipitation.*
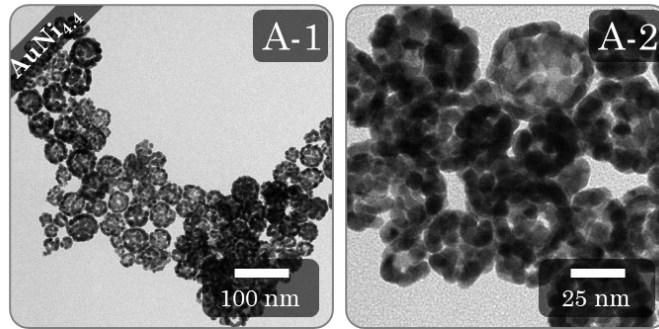
Figure 8: *AuNi$_{4.4}$ HS NPs synthesized with a prolonged initial degassing step (2 h) before the start of the galvanic replacement. This prolonged waiting time could lead to partial oxidation of the Ni NP surfaces resulting in a more fractured shell design. Otherwise, they show similar properties to the HS NPs with a shorter degassing time.*
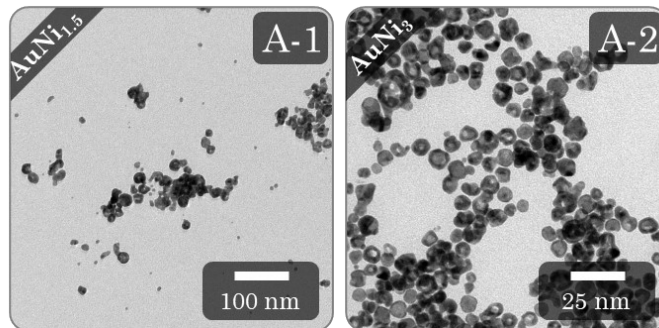

Figure 9: *HS NPs obtained by modifying the synthesis procedures from Cai et al. (A-1)[2] and Wang et al. (A-2)[3]. Both approaches rely on smaller initial Ni NPs than the approach from Shang et al.[4]. Although their smaller sizes make them auspicious, these HS NPs possess a fundamental disadvantage. As revealed by the TEM micrograph, they only appear in a mixture with solid nanoparticles, ring structures, and core-shell NPs. Additionally, for the approach according to Cai et al., an unidentifiable agglomerated mass is usually observed with only a small fraction of other structures.*
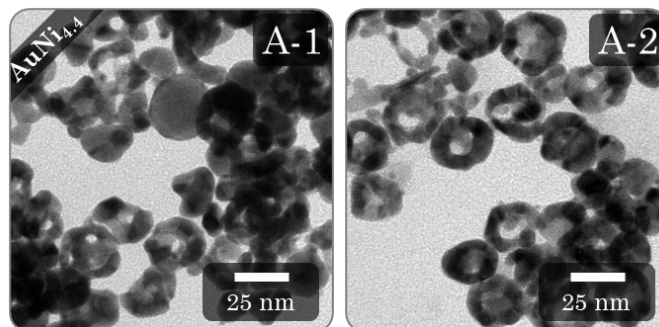

Figure 10: *AuNi$_{4.4}$ HS aerogel destabilized with 5 Eq. CaCl$_2$ (A-1) and BaCl$_2$ (A-2) without the centrifugation step. Both approaches lead to a building block diameter of ≈ 22 nm, which makes the destabilization process more gentle than centrifugation combined with NaBH$_4$. This also maintains the characteristic HS structure while allowing for a sufficient contact area. Therefore, a higher specific surface area and total pore volume are to be expected.*
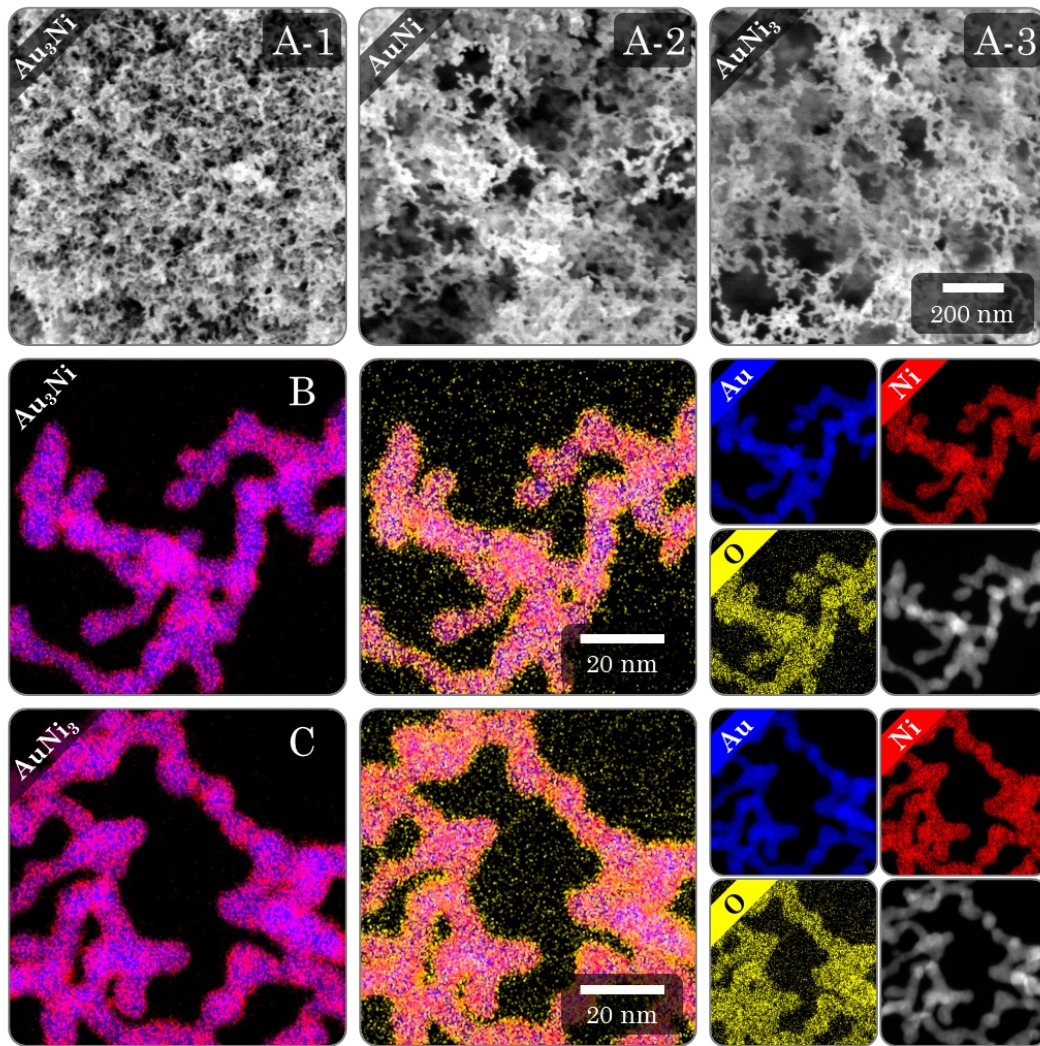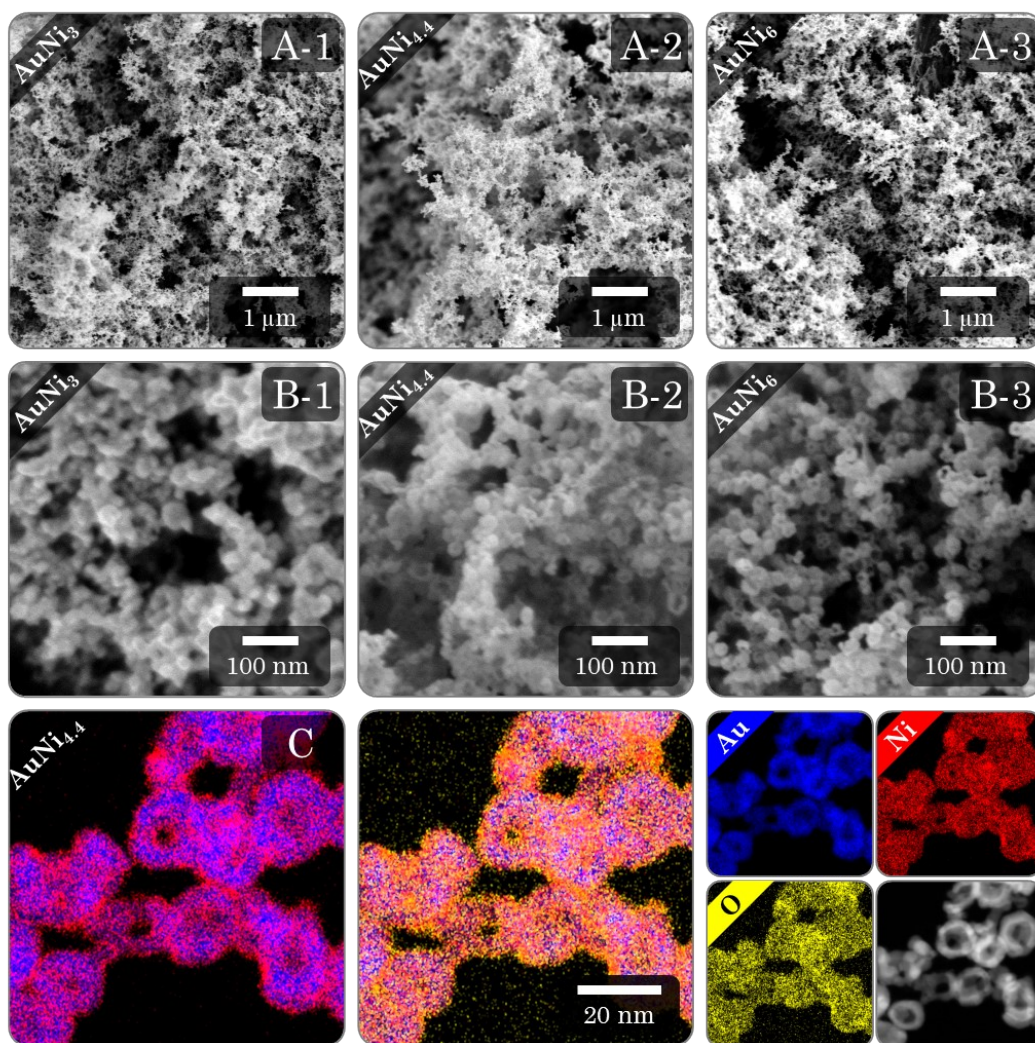
Figure 11: *(A) SEM micrographs of the Au₃Ni (1), AuNi (2), and AuNi₃ (3) alloy aerogels reduced by 12 Eq. NaBH₄. All samples show the typical three-dimensional sponge-like network. (B, C) HAADF-STEM imaging (lower right) and corresponding element distributions for the Au₃Ni (B) and AuNi₃ (C) aerogels. The element maps reveal a fairly homogeneous distribution of Au and Ni throughout the whole system (with a slight depletion of Ni in the interior of the ligaments) for both the Au- and Ni-rich gels. Additionally, the gel surface is covered by an oxide layer, causing a passivation effect.*
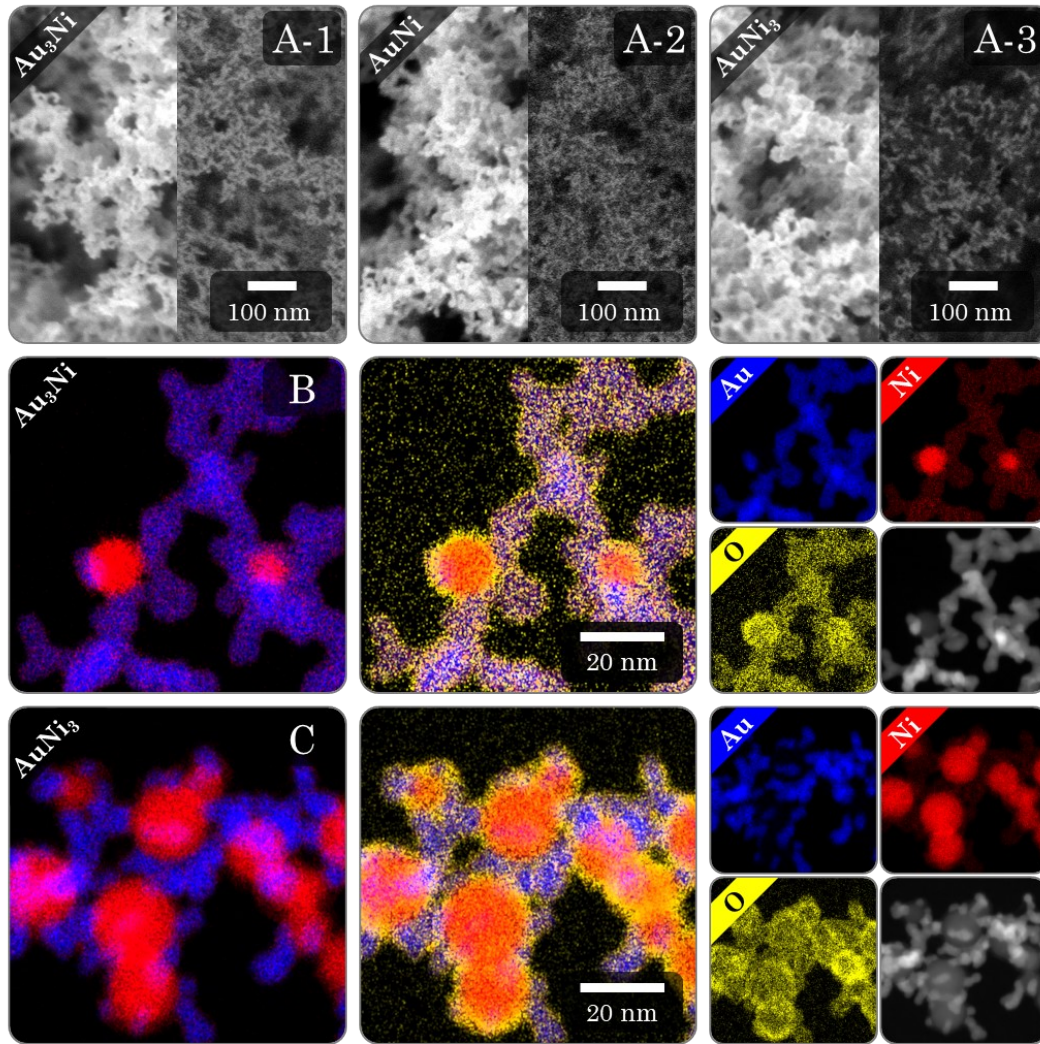
Figure 12: *(A) SEM micrographs from secondary electron (left) and backscattered electron imaging (right) of the Au$_3$Ni (1), AuNi (2), and AuNi$_3$ (3) heterostructure aerogels reduced by 12 Eq. NaBH$_4$. Besides the typical three-dimensional sponge-like network, the bipartite structure consisting of interconnected nanochains and nanoparticles is evident. This feature is especially pronounced in backscattering electron imaging. (B, C) HAADF-STEM imaging (lower right) and corresponding element distributions for the Au$_3$Ni (B) and AuNi$_3$ (C) aerogels. The element maps reveal thesegregation of Ni mainly into the nanoparticles, while Au is present only in the nanochains, doped with a small amount of Ni. As the Ni content increases, the number of NPs also increases, while the nanochain fragments become smaller. Additionally, the gel surface is again passivated by an oxide layer, which is significantly thicker for the Ni NPs than for the Au chains.*

Figure 13: *(A, B) SEM micrographs at different magnifications of the AuNi$_3$ (1), AuNi$_{4.4}$ (2), and AuNi$_6$ (3) aerogels destabilized by 5 Eq. NaBH$_4$. All samples show the typical three-dimensional sponge-like network. A closer inspection of the gel strands reveals the hollow-sphere character of the individual NP building blocks. (C) HAADF-STEM imaging (lower right) and corresponding element distributions for the AuNi$_{4.4}$ aerogel. The element maps reveal a homogeneous distribution of Au and Ni throughout the whole system, with an accumulation of Ni at the outer and inner surfaces of the HS NPs. Additionally, the gel surface is covered by an oxide layer similar to the alloy gels.*
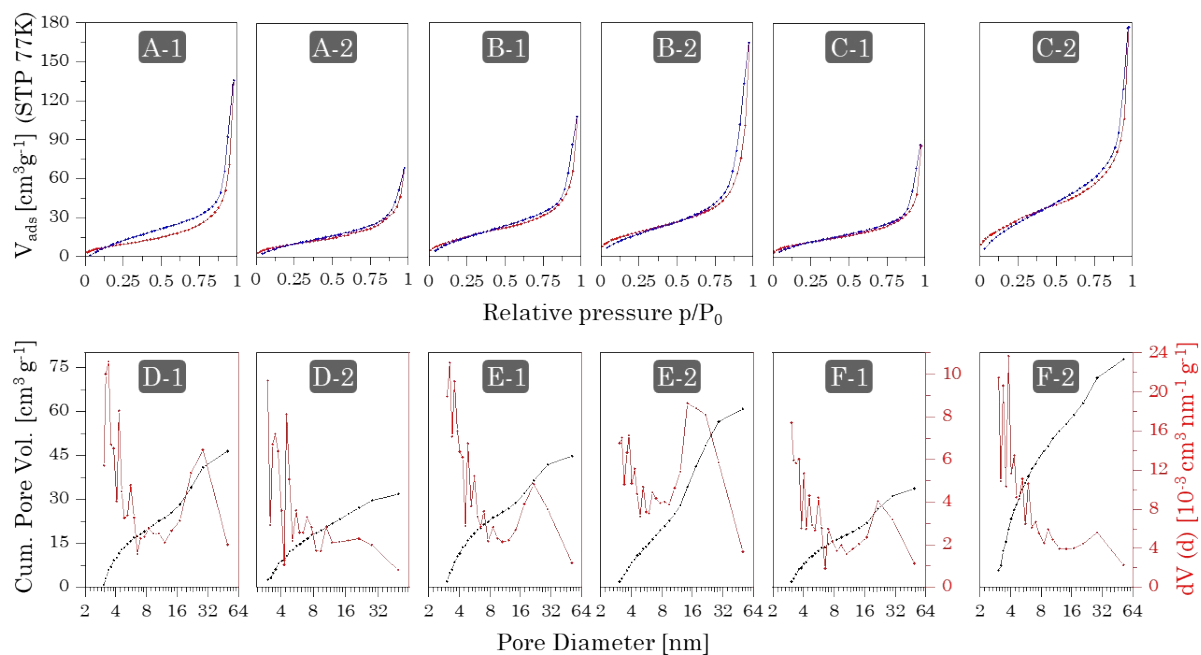
Figure 14: N_2 physisorption isotherms and pore size distributions of the $AuNi_6$ (A-1, D-1) and $AuNi_{4.4}$ (A-2, D-2) hollow sphere gels, the Au_3Ni (B-1, E-1) and $AuNi_3$ (B-2, E-2) heterostructure gels as well as the Au_3Ni (C-1, F-1) and $AuNi_3$ (C-2, F-2) alloy gels, measured at STP (standard temperature at 77 K and pressure). All isotherms show a characteristic mixture of Type II/IV behavior caused by the simultaneous presence of micro-, meso-, and macropores. Thereby, the HS gels exhibit a broader hysteresis. The pore size distribution is greatly influenced by the morphology. While the alloy gels have only a small amount of mesopores (with the exception of AuNi3 alloy gels), higher quantities are present for the HS and heterostructure gels in comparison, which is due to interior voids of the NPs and the interparticular voids created between the NPs and nanochains, respectively.

Table 1: *Final composition of selected representatives of all synthesized morphologies determined via SEM-EDX element analysis. The synthesized alloy and heterostructure aerogels show minor to small deviations from the nominal ratios, with a slight loss of Ni. This mismatch is likely due to the partial oxidation and dissolution of Ni, which increases with the initial Ni content and is more pronounced in the heterostructure gels. The HS gels show a severe deviation from the expected composition values caused by the oxidation of non-alloyed Ni.*

	Au_3Ni	$AuNi$	$AuNi_3$	$AuNi_{4.4}$	$AuNi_6$
Alloy	75.7 : 24.3	54.6 : 45.4	71.1 : 28.9		
Hetero-structure	80.7 : 19.3	58.9 : 41.1	34.6 : 65.4		
Hollow Sphere			89.2 : 10.8	89.1 : 10.9	83.6 : 16.4

Table 2: *Final compositions of the Au_2Ni heterostructure gels destabilized with different reducing agents. Only $NaBH_4$ was sufficient to preserve the initial metal composition inside the aerogel. For most other electrolytes, almost complete dissolution of Ni occurs. NaF represents a special case that retains some Ni, but still significantly less than $NaBH_4$.*

	Target [at%]		Final [at%]		
	Au	Ni	Au	Ni	Mn
$BaCl_2$	66.6	33.3	99.82	0.18	-
$CaCl_2$	66.6	33.3	99.74	0.26	-
$MnAc_2$	66.6	33.3	89.66	0.66	9.71
NaF	66.6	33.3	91.57	8.43	-
$NaBH_4$	66.6	33.3	66.1	33.9	-

References

1   M. Georgi, J. Kresse, K. Hiekel, R. Hübner and A. Eychmüller, *Catalysts*, 2022, **12**, 441–452.

2   B. Cai, A. Dianat, R. Hübner, W. Liu, D. Wen, A. Benad, L. Sonntag, T. Gemming, G. Cuniberti and A. Eychmüller, *Adv. Mater.*, 2017, **29**, 1605254–1605261.

3   M. Wang, W. Zhang, J. Wang, D. Wexler, S. D. Poynton, R. C. T. Slade, H. Liu, B. Winther-Jensen, R. Kerr, D. Shi and J. Chen, *ACS Appl. Mater. Interfaces*, 2013, **5**, 12708–12715.

4   C. Shang, W. Hong, J. Wang and E. Wang, *J. Power Sources*, 2015, **285**, 12–15.